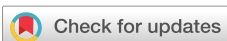


RESEARCH ARTICLE | DECEMBER 01 2020

## Chasing chaos by improved identification of suitable embedding dimensions and lags

Alessio Perinelli  ; Leonardo Ricci  



*Chaos* 30, 123104 (2020)

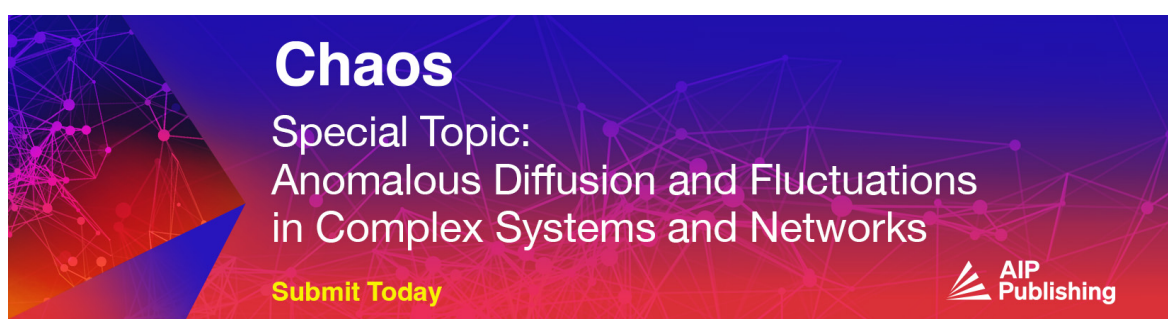
<https://doi.org/10.1063/5.0029333>



View  
Online



Export  
Citation



**Chaos**

Special Topic:  
Anomalous Diffusion and Fluctuations  
in Complex Systems and Networks

**Submit Today**

 AIP  
Publishing

# Chasing chaos by improved identification of suitable embedding dimensions and lags

Cite as: Chaos 30, 123104 (2020); doi: 10.1063/5.0029333

Submitted: 11 September 2020 · Accepted: 2 November 2020 ·

Published Online: 1 December 2020



Alessio Perinelli<sup>1</sup> and Leonardo Ricci<sup>1,2,a</sup>

## AFFILIATIONS

<sup>1</sup>Department of Physics, University of Trento, 38123 Trento, Italy

<sup>2</sup>CIMeC, Center for Mind/Brain Sciences, University of Trento, 38068 Rovereto, Italy

<sup>a</sup>Author to whom correspondence should be addressed: [leonardo.ricci@unitn.it](mailto:leonardo.ricci@unitn.it). URL: <http://nse.physics.unitn.it>

## ABSTRACT

The detection of an underlying chaotic behavior in experimental recordings is a longstanding issue in the field of nonlinear time series analysis. Conventional approaches require the assessment of a suitable dimension and lag pair to embed a given input sequence and, thereupon, the estimation of dynamical invariants to characterize the underlying source. In this work, we propose an alternative approach to the problem of identifying chaos, which is built upon an improved method for optimal embedding. The core of the new approach is the analysis of an input sequence on a lattice of embedding pairs whose results provide, if any, evidence of a finite-dimensional, chaotic source generating the sequence and, if such evidence is present, yield a set of equivalently suitable embedding pairs to embed the sequence. The application of this approach to two experimental case studies, namely, an electronic circuit and magnetoencephalographic recordings of the human brain, highlights how it can make up a powerful tool to detect chaos in complex systems.

Published under license by AIP Publishing. <https://doi.org/10.1063/5.0029333>

Complex nonlinear systems exhibit an irregular and aperiodic behavior that is due to either a stochastic source or a deterministic chaotic dynamics. The identification of chaos out of experimental recordings is a crucial, longstanding issue in nonlinear science because, besides improving the knowledge on the investigated system, it might help control and forecast its behavior. This search is pursued in many fields, from climate science to biology, physiology and neuroscience, with the goal of characterizing, for example, atmospheric dynamics, behavior of cells, physiological rhythms, and human brain activity. Here, we propose a new approach to detect chaos out of experimental recordings stemming from an unknown system. Our approach, which is tested on time series generated by an electronic circuit and by a human brain, makes up a new tool for the investigation of dynamical systems exhibiting complex behavior.

## I. INTRODUCTION

The detection of chaos is one of the key issues in the nonlinear analysis of time series generated by systems exhibiting aperiodic and unpredictable behavior such as the atmosphere,<sup>1–3</sup> financial markets,<sup>4,5</sup> single neurons,<sup>6,7</sup> the human heart,<sup>8–10</sup> and the human

brain.<sup>11–13</sup> Chaos is an appealing explanation for the irregularity and unpredictability of signals generated by these systems: a positive assessment of chaos implies an underlying deterministic mechanism ruling the system's dynamics, thus allowing forecasting at least on short time scales<sup>14</sup> as well as a better understanding of system properties.

Chaoticity is traditionally assessed by relying on two major properties of chaotic attractors, namely, the exponential divergence of nearby trajectories<sup>14</sup> and the fractal dimension of the attractor.<sup>15</sup> The former feature is usually ascertained by estimating the maximum Lyapunov exponent (MLE) via the divergence rate method.<sup>16–18</sup> The latter property is evaluated by quantifying estimators like the correlation dimension via the Grassberger–Procaccia scaling,<sup>19,20</sup> the box-counting dimension,<sup>15</sup> and the Kaplan–Yorke dimension.<sup>21,22</sup>

Most techniques devoted to the detection and characterization of chaos require the reconstruction of a proxy state space out of an input scalar sequence. The possibility of reconstructing the underlying dynamics out of a single observed variable is granted by Takens' theorem<sup>23,24</sup> and practically implemented by means of time delay embedding,<sup>25</sup> which requires the choice of a dimension  $m$  and a lag  $L$ . Optimally setting the two embedding parameters  $m, L$  is not a trivial task and prompted the development of many optimal embedding

criteria.<sup>26</sup> The crucial drawback of conventional methods for optimal embedding is their relying on arbitrary thresholds and on subjective evaluation of “limiting behaviors.”<sup>26</sup> As proposed by Pecora *et al.*,<sup>27</sup> a possible way to overcome these issues consists in formulating criteria that rely on statistical testing by replacing thresholds with probabilities; interpretation of results becomes more objective and robust. Moreover, traditional approaches to the problem of optimal embedding aim at providing a single pair  $m, L$  and, often, split the problem of choosing  $m$  and  $L$  into two separate problems.<sup>27</sup> Consequently, the role of the embedding window  $(m - 1)L T$  (where  $T$  is the sampling period), which has to comply with relevance and redundancy requirements,<sup>27,28</sup> is usually overlooked. (Throughout this work, the sampling period  $T$  is included within the product defining the embedding window.)

A recent work<sup>29</sup> describes the “embedding lattice method,” a new approach to the identification of suitable embedding dimensions and lags that overcomes the aforementioned issues. The approach relies on the analysis of an input sequence on a lattice of embedding pairs  $m, L$ , referred to as the “embedding lattice.” Two statistical tests allow a first identification and skimming of unsuitable pairs. Thereupon, correlation dimension is computed on each embedding pair by means of a novel estimator. The joint outcomes of the statistical tests and the correlation dimension estimation provide a *map* of the input sequence on the embedding lattice. The uniformity of the estimated correlation dimension within this map identifies a set of embedding pairs that are deemed to be suitable—and mutually statistically equivalent—to embed the input sequence. A suitable set of embedding pairs ends up to be constrained between two opposite time scales that are immediately interpretable in terms of redundancy and irrelevance times.<sup>28</sup> The analysis of sequences on a lattice of embedding pairs, which makes up the core idea underlying the embedding lattice method, is a change of paradigm with respect to the traditional approach of finding a single, supposedly optimal embedding pair  $m, L$ .

The goal of the present work is to investigate how the embedding lattice method can be used to detect chaos in experimental recordings. To this purpose, the reliability of embedding lattice maps is enhanced by integrating the method with a recently proposed, improved estimator of correlation dimension,<sup>30</sup> which relies on the asymptotic behavior of the so-called time dependent divergence exponent, i.e., the metric that is ordinarily used to estimate MLE out of scalar sequences. The improved estimator replaces the one introduced in the first formulation of the embedding lattice method.<sup>29</sup> The reliability of the identification of suitable sets of embedding pairs is then further enhanced by means of the assessment of the sample joint distribution of the embedding window and the correlation dimension. Here, we show that the implementation of these three steps makes up an analytical tool to characterize an input sequence and to investigate its possibly chaotic source. As a by-product, the implementation of the three steps also leads to an improved optimal embedding detection.

Three case studies are presented. The approach is first tested on a benchmark sequence generated by the Lorenz system. Experimental sequences generated by an implementation of Chua’s circuit are then analyzed; the related outcomes show the capabilities of the method in revealing chaos out of real-world recordings. Finally,

sequences corresponding to the brain activity in the resting state measured by magnetoencephalography (MEG) are investigated: in this case, no evidence of an underlying deterministic dynamics is present. While *absence of evidence is not evidence of absence*, this kind of analysis provides a powerful, first-hand tool to evaluate the suitability of time sequences in the quest for chaos within a complex system, as well as the adequacy of the sampling experimental setup.

The present work is organized as follows. Section II describes the characterization of the possibly chaotic source by means of an improved method for the identification of suitable embedding parameters and its test on a benchmark Lorenz system. In Sec. III, the new approach to detect chaos is applied to experimental recordings, and the related outcomes are discussed. Concluding remarks are drawn in Sec. IV. For the sake of readability and clarity, mathematical details and computational costs of their implementation are discussed in the Appendix.

## II. CHAOS DETECTION VIA IMPROVED IDENTIFICATION OF SUITABLE EMBEDDING DIMENSIONS AND LAGS

The starting point of our approach is a scalar sequence  $\{y_n\}$  generated by a system that, in a quest for chaos, is hypothesized to be finite-dimensional and chaotic.

### A. Three-steps for improved identification of suitable embedding dimensions and lags

The scalar sequence  $\{y_n\}$  is supposed to be standardized as  $y \rightarrow (y - \bar{y})/\sigma$ , where  $\bar{y}$  and  $\sigma$  are the sequence’s sample mean and sample standard deviation, respectively. The parameter space of the embedding lattice method,<sup>29</sup> namely, the embedding lattice, is defined as the set of embedding pair  $\{m, L | m \in [2, m_{\max}], L \in [1, L_{\max}]\}$ . Setting the lattice boundaries  $m_{\max}, L_{\max}$  requires a trade-off between the necessity to overcome the redundancy time scale, which requires embedding windows to be large enough, and the combination of computational cost, irrelevance time scale, and length of the available input sequence, which make unpractical or useless the analysis of very large values of  $m, L$ . More in detail, the embedding windows  $(m - 1)L T$  have to explore the whole time scale range between  $\tau_R$  and  $\tau_I$ . Consequently,  $m_{\max}L_{\max}T$  has to be larger than  $\tau_I$ , i.e.,  $m_{\max}L_{\max} > \tau_I/T$ . However, because of Nyquist-Shannon sampling theorem, the sampling time  $T$  has to comply with the constraint  $\frac{1}{T} > 2f_{\max} \approx \frac{1}{\tau_R}$ , where  $f_{\max}$  is the upper significant boundary of the input sequence spectrum. This last constraint corresponds to the ability to observe the lower boundary of the uniformity region defined below in step 3. Merging the two conditions leads to the following constraint,  $m_{\max}L_{\max} > \tau_I/\tau_R$ , which corresponds to the ability to observe and explore the whole uniformity region. Unfortunately, and especially when an unknown input sequence is given, the ratio  $\tau_I/\tau_R$  cannot be generally evaluated *a priori*, not even by using spectral analysis. On the other hand, the lower bound to  $m_{\max}L_{\max}$  hints at the uselessness of setting too a large value of  $m_{\max}L_{\max}$ , also taking into account the related computational cost. We have found that, once the sampling period  $T$  is properly chosen, a sound compromise to explore the uniformity region is to set  $m_{\max} = 20, L_{\max} = 20$ .

According to the embedding lattice method, sample correlation integrals are evaluated for each embedding pair  $m, L$  belonging to the embedding lattice. It is worth recalling that a correlation integral is a sample cumulative distribution  $\widehat{C}_{m,L}(\delta)$  of a distance  $\delta$  in the set  $\{\mathbf{Y}_n\}$  of vectors that make up the embedded sequence, where  $\mathbf{Y}_n = (y_n, y_{n+L}, \dots, y_{n+(m-1)L})$ . Details of how correlation integrals are evaluated are provided in the [Appendix](#).

Remarkably, by subtracting  $\delta$  to a sample correlation integral, a sample “correlation bridge”  $\widehat{B}_{m,L}(\delta)$  is obtained,  $\widehat{B}_{m,L}(\delta) = \widehat{C}_{m,L}(\delta) - \delta$ , which, in the case of a Gaussian white noise (GWN) source, turns out to correspond to a Brownian bridge. This last property allows for the implementation of the first two evaluation steps, which act on sample correlation bridges as follows.

1. Compatibility of the sequence with a GWN source. As summarized in the [Appendix](#), the compatibility is assessed via a Kolmogorov–Smirnov test to check whether the correlation bridge is Brownian (typically,  $p$  value  $>0.01$ ). Embedding pairs for which compatibility holds “see” the input sequence as a GWN one. In a quest for chaos, they are deemed to be unsuitable to embed the sequence and, therefore, discarded from further evaluations.

2. Compatibility of the sequence with a finite-dimensional source. For a source with finite dimension, correlation bridges turn out to diverge at the origin, provided that the embedding dimension is larger than the correlation dimension.<sup>29</sup> As discussed in the [Appendix](#), the divergence is essentially a gauge-transformed, equivalent formulation of the Grassberger–Procaccia scaling at small distances. Embedding pairs for which incompatibility holds are characterized by either a deficient  $m$  with respect to the unknown correlation dimension  $\nu$  of the chaotic source ( $m < \nu$ ) or by an excessive embedding window with respect to the irrelevance time  $\tau_I$ :  $m > \tau_I/(LT)$ . The former case hints at a high-dimensional chaotic source or even a stochastic one. The latter case, on the other hand, corresponds to the absence of any correlation among the elements of each embedding vector. Consequently, embedding vectors are scattered within the embedding space and do not probe in any “relevant” way the underlying system’s trajectory.<sup>31</sup> In both cases, the embedding pairs are discarded from further evaluation.

The loss of correlation among the elements of each embedding vector is not an abrupt process when  $m$  is tuned across  $\tau_I/(LT)$ : once this threshold is overcome, the embedding points still “see” a finite-dimensional system, which, however, appears to be more noisy due to the loss of correlation and, therefore, with a larger sample correlation dimension. Further increasing  $m$  eventually leads the reconstructed system to become incompatible with a finite-dimensional hypothesis. It follows that boundaries between regions in which compatibility and incompatibility holds cannot be used to assess the irrelevance time, which, however, can be estimated by using step 3, as discussed below.

The third, final evaluation step relies on the determination of the sample correlation dimension  $\widehat{\nu}$  out of the input sequence. The determination is carried out only for those embedding pairs that survived the two previous steps. Crucially, in the present work, the sample correlation dimension  $\widehat{\nu}$ , rather than being estimated directly from the correlation bridges,<sup>29</sup> is assessed by using an improved, recently introduced technique, which is also outlined in the [Appendix](#). Thereupon, the third step is implemented as follows.

3. Identification of “uniformity regions” of the embedding lattice that show a uniform  $\widehat{\nu}$  and whose corresponding embedding window  $(m-1)LT$  lays between two boundaries corresponding to the redundancy time  $\tau_R$  and the irrelevance time  $\tau_I$ , with  $\tau_I > \tau_R$ . The identification relies on the analysis of the distribution of  $\widehat{\nu}$  on the embedding lattice as well as of the sample joint distribution of the sample correlation dimension  $\widehat{\nu}$  and the embedding window  $(m-1)LT$ . This third step is the crucial one for the detection of a possible underlying chaotic dynamics.

## B. Chaos detection

The new approach to detect chaos is here described by using the Lorenz system as a prototypical example. [Figure 1](#) shows, in terms of a map of the sample correlation dimension  $\widehat{\nu}$  and the related histogram, the results of the three evaluation steps described above in the case of a synthetic sequence generated by integrating the Lorenz system,<sup>32</sup> namely,  $\dot{x} = \sigma(y - x)$ ,  $\dot{y} = x(r - z) - y$ ,  $\dot{z} = xy - bz$ . System parameters are set to  $\sigma = 10$ ,  $r = 28$ ,  $b = 8/3$ . Upon randomly setting the starting point, differential equations were integrated via a Runge–Kutta Prince–Dormand (8,9) algorithm with integration step  $dt = 0.03$ , which is also taken as the sampling time  $T$ . The sequence to analyze corresponds to  $10^5$  samples of the  $x$  coordinate of the system.

Despite its well-known origin, in the following the sequence is supposed to stem from an unknown system, which, according to the first assumption of our approach, is deemed to be finite-dimensional and chaotic. As a result of the statistical test of step 1, no embedding pair “sees” the input sequence as stemming from a GWN source. Following step 2, there are embedding pairs—marked with a “+” sign within [Fig. 1\(a\)](#)—whose  $m$  is less than the system’s correlation dimension  $\nu$  or, alternatively, whose corresponding embedding window overcomes the system’s irrelevance time  $\tau_I$ . These embedding pairs occur at  $m = 2$ , which is indeed an inadequate dimension to embed the Lorenz system, and at large  $m$  and  $L$ , for which the embedding window becomes too large [see upper-right corner of [Fig. 1\(a\)](#)]. As explained in Sec. II A, overcoming the system’s irrelevance time is characterized by, first, an increased estimated  $\widehat{\nu}$ , and then, for larger embedding windows, an incompatibility with a finite-dimensional source (step 2). As a consequence of step 3, the embedding lattice map of [Fig. 1\(a\)](#) shows a region in which the sample correlation dimension  $\widehat{\nu}$  takes on a uniform value. Many of the lattice points corresponding to embedding windows greater than 6 were discarded due to an excessive computational time for the assessment of  $\widehat{\nu}$ . As shown below, the exclusion of these points does not affect the analysis. The computational time turns out to be approximately proportional to the embedding window. For practical reasons, an upper limit of 6 h was set. Further details on computational costs are given at the end of the [Appendix](#).

A region of uniformity of  $\widehat{\nu}$  is highlighted by the histogram in [Fig. 1\(b\)](#): the peak corresponds to the histogram bin characterized by  $\widehat{\nu} = 2.05 \pm 0.05$  and to the region bounded by the black, solid line in [Fig. 1\(a\)](#). It is worth noting that the histogram peak is narrower compared to the similar assessment carried out in the first formulation of the embedding lattice method,<sup>29</sup> as a consequence of the use of the improved correlation dimension estimator. Importantly, the uniformity region turns out to be bounded by two hyperbolae, each

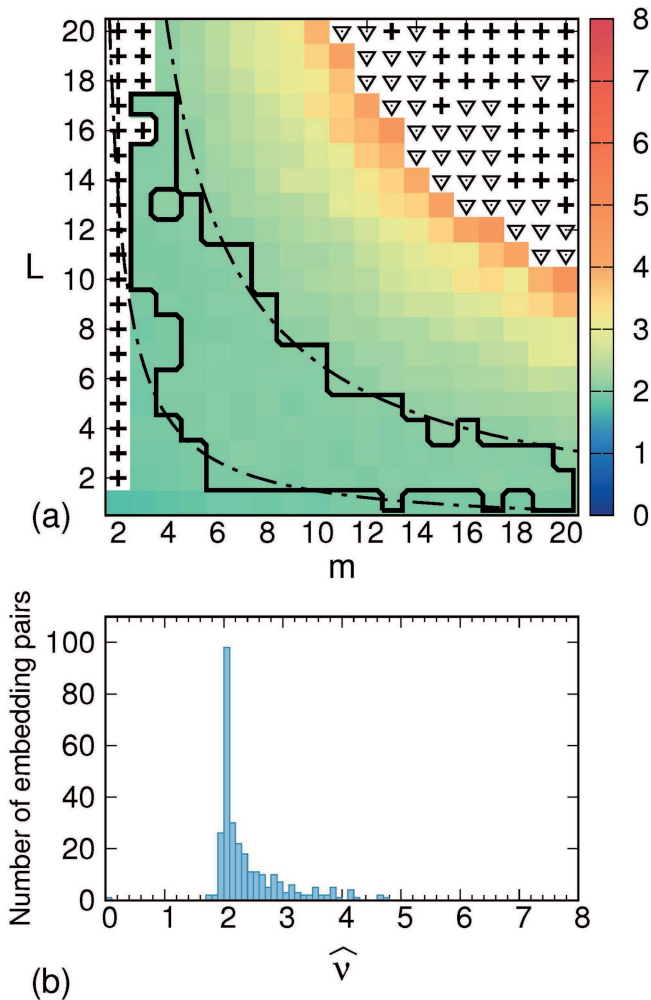


**FIG. 1.** (a) Results of the three analytical steps carried out on a Lorenz sequence and using an embedding lattice  $[2, 20] \times [1, 20]$ . No embedding pair was ruled out because of a compatibility with a GWN source (step 1). Embedding pairs marked with a "+" sign provide incompatibility with the requirements of step 2, namely,  $v \leq m \leq \tau_I/(LT)$ . With regard to step 3, black triangles correspond to embedding pairs for which an evaluation of  $\hat{v}$  is unavailable due to the algorithm exceeding a computational time limit of 6 h (see the main text). On the remaining points, a map of estimated  $\hat{v}$  is shown. (b) Histogram of the estimated  $\hat{v}$ : the bin width is 0.1. The black solid line in (a) encompasses the lattice region corresponding to the histogram peak at  $\hat{v} = 2.05 \pm 0.05$ . The black dashed-dotted curves are two hyperbolae bounding the region of uniform  $\hat{v}$  and defined by  $(m-1)LT \simeq 0.4$ ,  $(m-1)LT \simeq 1.8$ .

characterized by a value of the embedding window  $(m-1)LT$ . The two values can be respectively interpreted as the redundancy time  $\tau_R \simeq 0.4$  and the irrelevance time  $\tau_I \simeq 1.8$ .

The identification of a uniformity region is indeed a crucial task: although histograms of  $\hat{v}$  can highlight the presence of a uniformity region, spurious peaks can mislead this evaluation. In other words, the question is whether a peak in the histograms of  $\hat{v}$  indeed

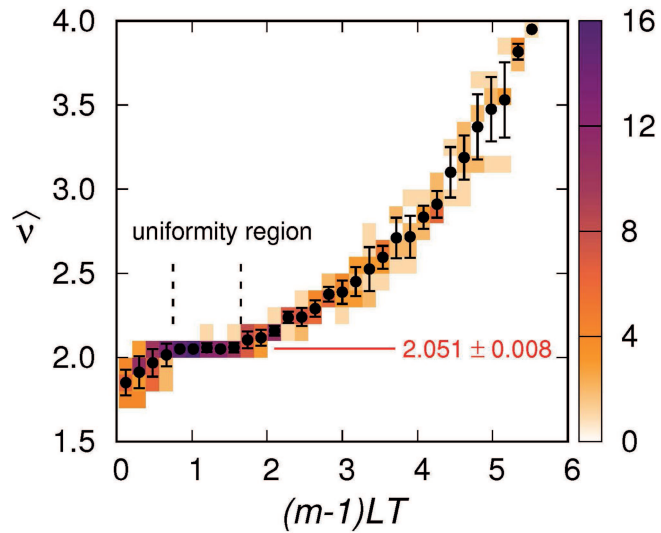


**FIG. 2.** Sample joint distribution of  $(m-1)LT$ ,  $\hat{v}$  for the correlation dimension map built out of the Lorenz sequence and shown in Fig. 1. Bin width is 0.1 along the  $\hat{v}$  axis and 0.18 along the  $(m-1)LT$  axis. Black dots and the related error-bars correspond to the expected value and the related uncertainty of  $\hat{v}$  for each given value (bin) of the embedding window. A uniformity region can be identified corresponding to embedding windows between 0.75 and 1.65. Averaging  $\hat{v}$  within the uniformity region yields  $2.051 \pm 0.008$ .

corresponds to a uniformity region within the lattice (as it is the case in several examples of Sec. III B). The identification is improved by assessing a sample joint distribution of the embedding window  $(m-1)LT$  and the sample correlation dimension  $\hat{v}$ . The sample joint distribution for the map in Fig. 1 concerning the Lorenz sequence is shown in Fig. 2. In the embedding window interval between the values 0.75 and 1.65—which improve the previous, rough assessments of  $\tau_R$ ,  $\tau_I$ , respectively—the sample correlation dimension takes on a constant value: averaging this quantity within a uniformity region yields  $2.051 \pm 0.008$ .

It is worth comparing the set of suitable embedding parameters identified by the present approach with those resulting by the implementation of possibly the most widespread method to assess optimal embedding, namely, the joint application of mutual information and false nearest neighbors.<sup>26</sup> According to the former criterion, an optimal lag  $L$  is identified as the first minimum of the sequence's mutual information.<sup>33,34</sup> Thereupon, an optimal dimension  $m$  is determined by assessing the fraction of false nearest neighbors as a function of  $m$  and by selecting the value for which this fraction vanishes.<sup>14,26</sup> Both algorithms are here implemented by relying on the routines provided within the TISEAN package.<sup>35,36</sup> The resulting optimal embedding parameters for the Lorenz sequence are  $m = 7$ ,  $L = 6$ . This embedding point lays within the uniformity region highlighted in Fig. 1(a).

In conclusion, one can affirm that the input sequence is compatible with the assumption of a source being finite-dimensional and chaotic. In addition, an optimal embedding region is identified,

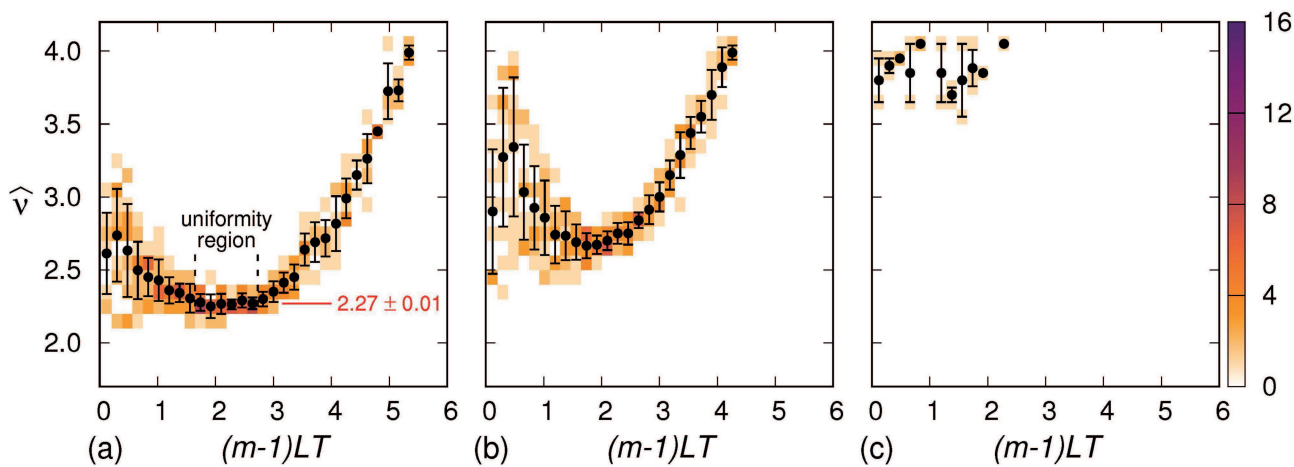


**FIG. 3.** Sample joint distributions of  $(m-1)LT$ ,  $\hat{v}$  for the correlation dimension map built out of the Lorenz sequence tainted with observational noise. Bin width is 0.1 along the  $\hat{v}$  axis and 0.18 along the  $(m-1)LT$  axis. Black dots and the related errorbars correspond to the expected value and the related uncertainty of  $\hat{v}$  for each given value (bin) of the embedding window. (a) In the case of a noise-affected sequence with SNR equal to 30 dB a uniformity region can still be identified, corresponding to embedding windows between 1.65 and 2.73. Averaging  $\hat{v}$  within the uniformity region yields  $2.27 \pm 0.01$ . (b) In the case of a noise-affected sequence with SNR equal to 20 dB, no uniformity region can be identified. (c) In the case of a noise-affected sequence with SNR equal to 10 dB, most points of the lattice are discarded as a consequence of step 2.

05 April 2024 16:52:55

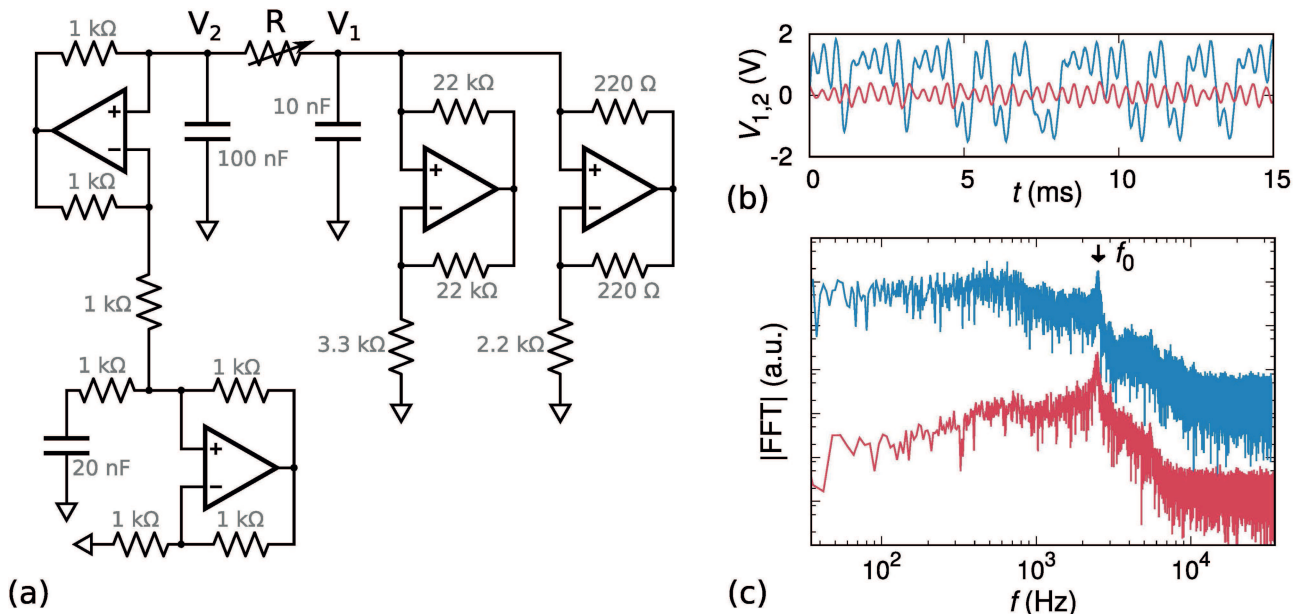


**FIG. 4.** (a) Implementation of Chua's circuit by using four OP-07 operational amplifiers.<sup>46</sup> The two rightmost operational amplifiers make up the nonlinear Chua diode, while the two leftmost ones act as a gyrator to convert the  $20\text{ nF}$  capacitor into an effective  $20\text{ mH}$  inductor. Values of resistors and capacitors are reported. The variable resistor  $R$  corresponds to a  $10\text{ k}\Omega$  trimmer. Recorded signals correspond to the potentials  $V_1$ ,  $V_2$ . (b) Sample, 15 ms long sequence of  $V_1$  (blue line) and  $V_2$  (red line). (c) Fourier spectrum of  $V_1$  (blue line) and  $V_2$  (red line). Both Fourier spectra present a peak at  $f_p \cong 2.5\text{ kHz}$ , corresponding to the typical oscillation frequency observable in the sequence plots. (The Fourier spectrum of  $V_2$  is shifted downwards for the sake of clarity.)

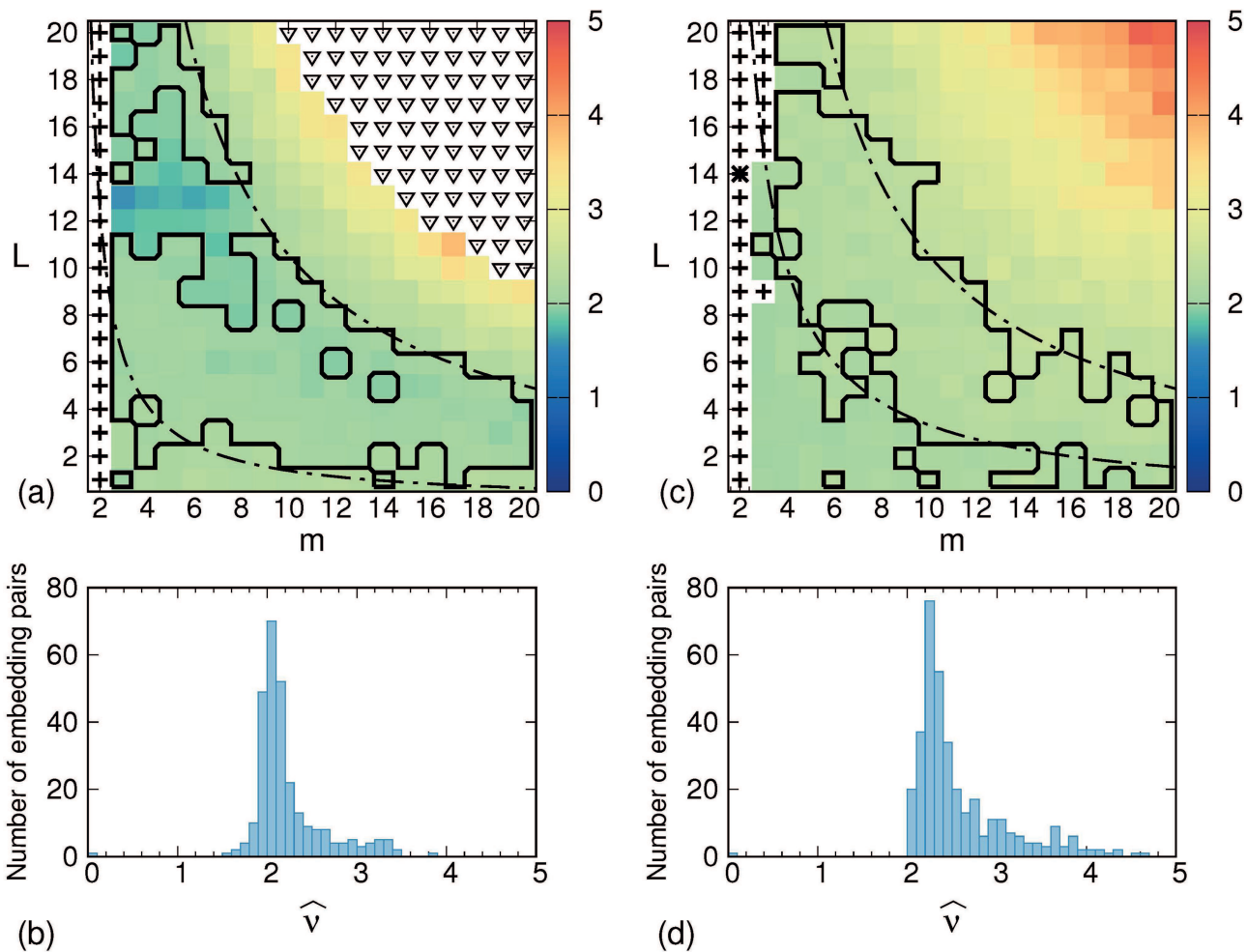


**FIG. 5.** Results of the three analytical steps carried out on (a) a sequence of 33 334 points sampled at  $T = 15 \mu\text{s}$  of the potential  $V_1$  and (c) a sequence of  $10^5$  points sampled at  $T = 5 \mu\text{s}$  of the potential  $V_2$  of Chua's circuit (see Fig. 4). The embedding lattice is  $[2, 20] \times [1, 20]$ . As a result of step 1, in the first case, no embedding pair shows a compatibility with a GWN source, while in the second case the embedding pair  $(2, 14)$  does. Consequently, this pair was ruled out by further evaluations. Embedding pairs marked with a "+" sign provide incompatibility with the requirements of step 2, namely,  $v < m < \tau_1/(LT)$ . With regard to step 3, black triangles correspond to embedding pairs for which an evaluation of  $\hat{v}$  is unavailable due to the algorithm exceeding a computational time limit of 6 h. On the remaining points, the maps of estimated  $\hat{v}$  are shown. A "gap" is apparent at  $L \approx 13 \pm 1$  and  $m \leqslant 7$ . (b) and (d) Histograms of the estimated  $\hat{v}$  in the case of the  $V_1$  and the  $V_2$  sequence, respectively; in both cases, the bin width is 0.1. The black solid line in (a) encompasses the lattice region corresponding to the histogram peak in (b) at  $\hat{v} = 2.05 \pm 0.10$ . The black solid line in (c) encompasses the lattice region corresponding to the histogram peak in (d) at  $\hat{v} = 2.3 \pm 0.1$ . The black dashed-dotted curves in (a) are two hyperbolae bounding the region of uniform  $\hat{v}$  and defined by  $(m - 1)L T \simeq 0.2 \text{ ms}$ ,  $(m - 1)L T \simeq 1.4 \text{ ms}$ . The black dashed-dotted curves in (c) are two hyperbolae bounding the region of uniform  $\hat{v}$  and defined by  $(m - 1)L T \simeq 0.15 \text{ ms}$ ,  $(m - 1)L T \simeq 0.5 \text{ ms}$ .

which delivers a value of the correlation dimension in perfect compliance with the source of the analyzed sequence, i.e., the Lorenz system. The assessed correlation dimension is in agreement with conventional assessments made by applying the standard Grassberger–Procaccia method<sup>34,37</sup> and improves the uncertainty by more than one order of magnitude: while the value obtained here is  $2.051 \pm 0.008$ , the estimated value assessed in the first formulation of the embedding lattice method<sup>29</sup> is  $2.0 \pm 0.2$ ; moreover, the value obtained by Sprott and Rowlands through an *improved correlation dimension calculation*<sup>37</sup> is  $2.049 \pm 0.096$ . It is worth mentioning that,

in the paper where the algorithm for the estimation of correlation dimension was first introduced,<sup>19</sup> Grassberger and Procaccia quoted a value equal to  $2.05 \pm 0.01$  for the Lorenz system, although they also stated that *errors quoted are educated guesses*.

### C. Chaos detection and observational noise

This section is devoted to the test of our approach in the case of sequences affected by observational noise. To address this issue, a Lorenz sequence was tainted by using different levels

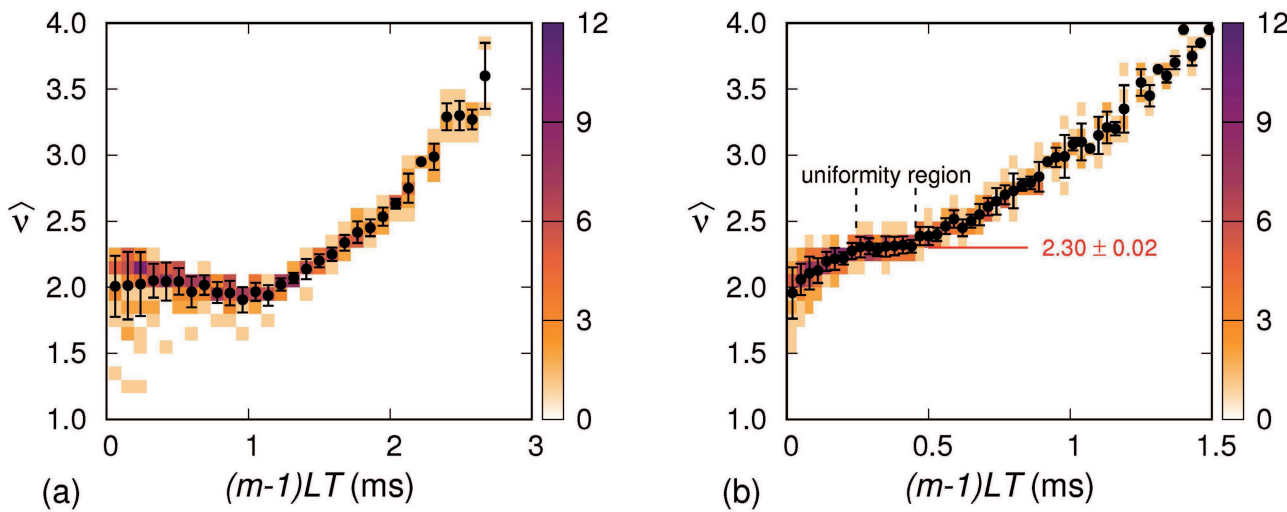


**FIG. 6.** Sample joint distributions of  $(m-1)LT$ ,  $\hat{v}$  for the correlation dimension maps built out of the recorded potentials  $V_1$  (a) and  $V_2$  (b) of Chua's circuit shown in Fig. 5. Bin width is 0.1 along the  $\hat{v}$  axis in both cases and, along the  $(m-1)LT$  axis, 90  $\mu\text{s}$  in (a) and 30  $\mu\text{s}$  in (b). Black dots and the related errorbars correspond to the expected value and the related uncertainty of  $\hat{v}$  for each given value (bin) of the embedding window. In the case of  $V_1$ , the drop of  $\hat{v}$  for values of the embedding window between 0.4 and 1 is due to the presence of the gap in Fig. 5(a). In the case of  $V_2$ , a uniformity region can be identified corresponding to embedding windows between 0.245 and 0.455. Averaging  $\hat{v}$  within the uniformity region yields  $2.30 \pm 0.02$ .

of observational noise. The elements  $s_n$  of a noise-affected input sequence are given by

$$s_n = x_n + \eta_n,$$

where  $x_n$  are the elements of a Lorenz sequence, while the noise contributions  $\eta_n$  are i.i.d. random variates distributed according to  $\eta_n \sim \mathcal{N}(0, \sigma_\eta^2)$ . A sequence's SNR is defined (in decibels) as

$$\text{SNR} = 20 \text{ dB } \log_{10} \left( \frac{\sigma_x}{\sigma_\eta} \right),$$

where  $\sigma_x = 7.93$  is the standard deviation of the Lorenz sequence  $\{x_n\}$  used in this work. The sequences considered here have SNR equal to 30 dB, 20 dB, and 10 dB. The corresponding sample joint distributions of the embedding window  $(m-1)LT$  and the sample correlation dimension  $\hat{v}$  are shown in Fig. 3. A uniformity region can be identified up to a SNR of 30 dB, although the corresponding estimated  $\hat{v}$  is  $\sim 15\%$  higher than in the noiseless case. The noise contamination has the effect of increasing the dimensionality of the observed system. For higher values of SNR, the uniformity region is washed out, as shown in Fig. 3(b). Eventually, most embedding points turn out to be discarded as a consequence of step 2, as shown in Fig. 3(c). In this last case, the sequence is seen as being infinite dimensional. In conclusion, the prototypical case provided by the Lorenz sequence can be still identified as a chaotic one until a signal-to-noise ratio of about 30 dB.

### III. CHASING CHAOS IN EXPERIMENTAL RECORDINGS

In the following, the application of the chaos detection approach is discussed for two real-world case studies: a chaotic

electronic circuit and MEG recordings of the human brain resting-state activity.

#### A. Chua's circuit

Electronic circuits are versatile platforms that allow us to generate and study different—possibly chaotic—dynamical regimes.<sup>38–43</sup> Figure 4 shows an implementation of Chua's circuit<sup>44</sup> relying on four operational amplifiers. Two op-amps implement Chua's diode, which provides the basic nonlinear circuit element having a piecewise-linear current–voltage characteristic. The inductor of the canonical Chua's circuit implementation<sup>45</sup> is here replaced by a gyrator network that converts a capacitor impedance into an inductor one by means of two op-amps. Here, two signals are considered, namely, the potential  $V_1$  and  $V_2$  at the two pins of the resistor  $R$ . Adjusting the variable resistor allows us to reach different dynamical regimes: from periodic oscillations to, in the range between 1.7 k $\Omega$  and 1.8 k $\Omega$ , a *presumptive*—as it results by looking at  $V_1$ – $V_2$  Lissajous figures—chaotic regime.

The potentials  $V_1$  and  $V_2$  are sampled each  $T = 5 \mu\text{s}$  on a time span of 0.5 s, leading to two sequences of  $10^5$  points each. To highlight the versatility of the approach described in this paper, the sequence corresponding to  $V_1$  is downsampled by a factor 3 so that its length is reduced to 33 334 points, with a sampling period of 15  $\mu\text{s}$ . The analysis of Sec. II is then performed on both recorded sequences of  $V_1$  and  $V_2$ .

Figure 5 shows the results of the map analysis. For both  $V_1$  and  $V_2$ , the presence of a hyperbolae-bounded embedding lattice region, which corresponds to a uniform value of the sample correlation dimension  $\hat{v}$ , hints at the presence of chaos. In the case of  $V_1$ , sample correlation dimension for most embedding points corresponding to

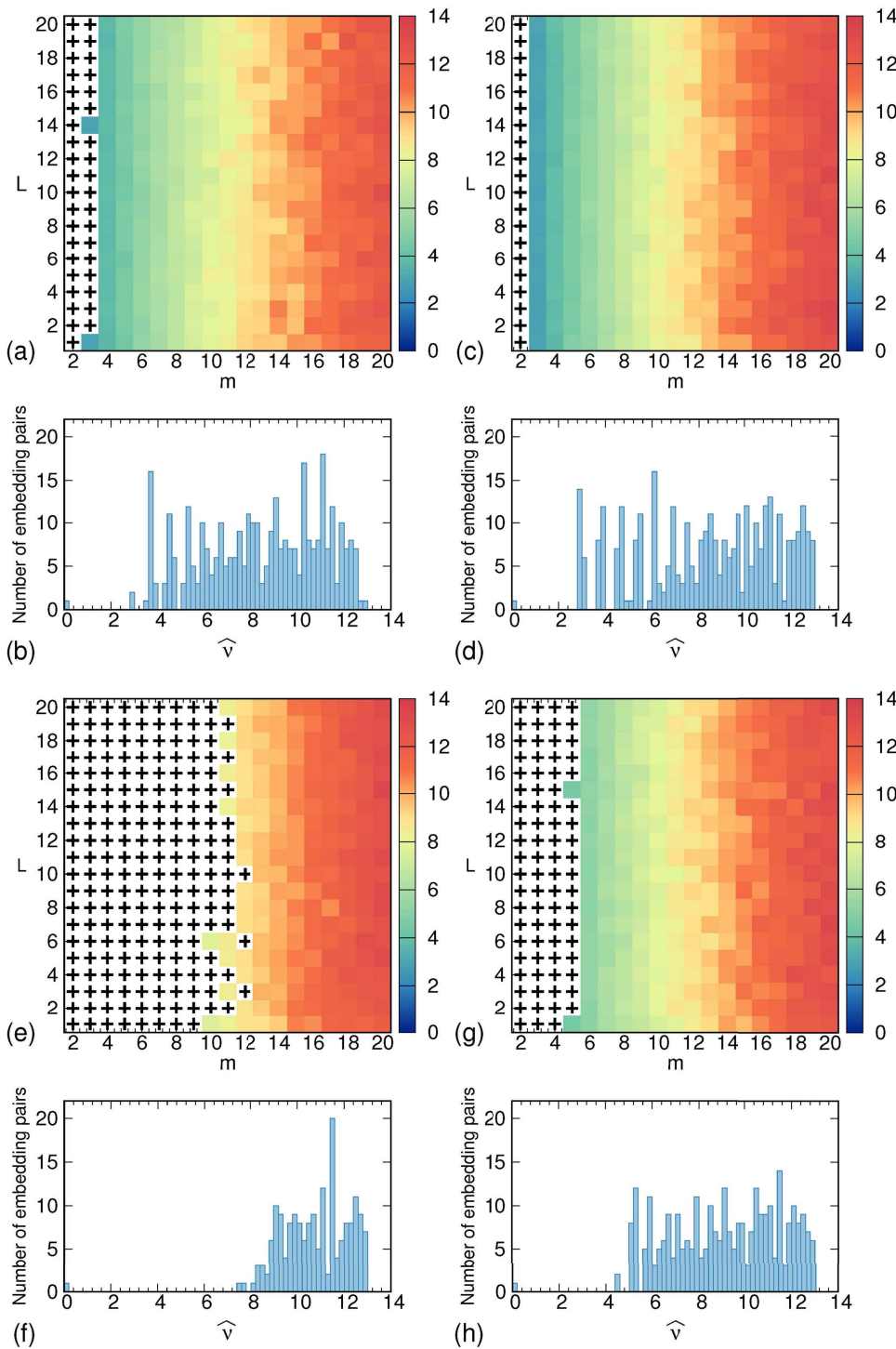


**FIG. 7.** Results of the three analytical steps carried out on current dipole sequences corresponding to the brain locations 10pp (a), V4 (c), 5m (e), and STGa (g). The embedding lattice is  $[2, 20] \times [1, 20]$ . No embedding pair was ruled out because of a compatibility with a GWN source (step 1). Embedding pairs marked with a "+" sign provide incompatibility with the requirements of step 2, namely,  $v < m < \tau_1/(LT)$ . With regard to step 3, the maps of  $\hat{v}$  estimated on the remaining points are shown. (b), (d), (f), and (h) Histograms of the estimated  $\hat{v}$  in the case of the 10pp, V4, 5m, and STGa sequences, respectively; in all cases, the bin width is 0.2.

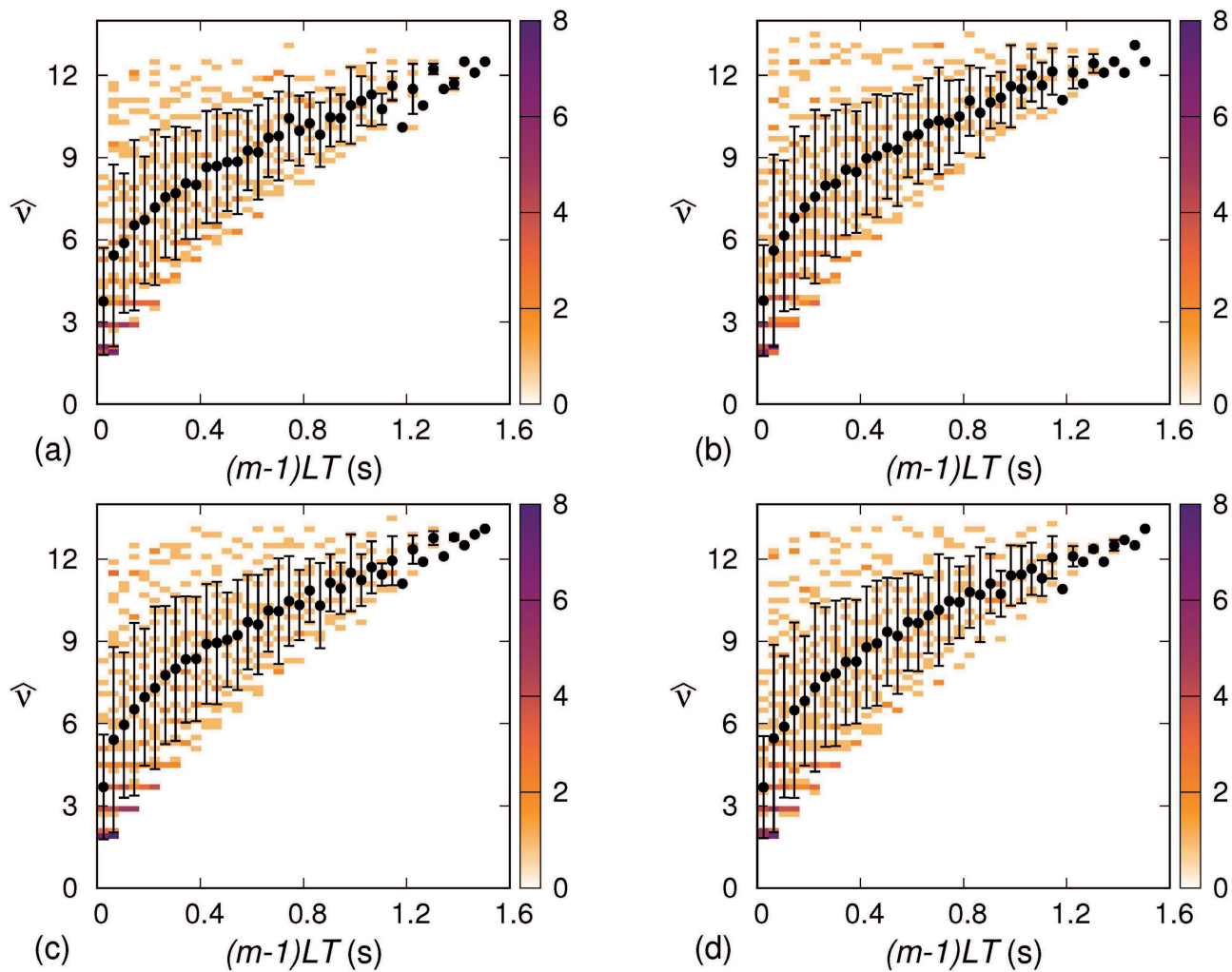


**FIG. 8.** Sample joint distributions of  $(m - 1)LT, \hat{v}$  for the correlation dimension maps built out of current dipole sequences corresponding to the brain locations 10pp (a), V4 (b), 5m (c), STGa (d) and shown in Fig. 7. Bin width is 0.2 along the  $\hat{v}$  axis in all cases and 40 ms along the  $(m - 1)LT$  axis. Black dots and the related errorbars correspond to the expected value and the related uncertainty of  $\hat{v}$  for each given value (bin) of the embedding window.

embedding windows larger than 3 ms was not computed because the corresponding computational time exceeded the upper limit of 6 h mentioned above.

The uniformity region of  $V_1$  is actually disconnected by a “gap” occurring at  $L = 13 \pm 1$ , i.e.,  $LT \approx (200 \pm 15) \mu\text{s}$ , and  $m \leq 7$ . The gap is due to the fact that the embedding highlights more the periodical behavior of the system than its chaotic feature: the product  $LT \approx 200 \mu\text{s}$  corresponds to half the typical period of the oscillator, namely,  $f_p^{-1} \approx 400 \mu\text{s}$ , where  $f_p$  is defined in the caption to Fig. 4. This setting predominantly yields embedding vectors that, at least for small dimension  $m$ , have components that are alternatively and approximately equal to  $\pm 1$  times a constant. Consequently, the embedding tends to project the state space onto a vector  $(1, -1, 1, \dots)$ , i.e., to a unidimensional subspace. This fact is

substantiated by the values of  $\hat{v}$  within the gap, i.e., at  $m \leq 7, L = 13$ , ranging between 1.6 and 1.7. As a consequence of the gap, the sample joint distribution of the embedding window  $(m - 1)LT$  and the sample correlation dimension  $\hat{v}$  shown in Fig. 6(a) does not allow for the identification of a uniformity region.

On the other hand, the uniformity region of  $V_2$ , due to a sampling frequency three times higher than  $V_1$ , shows a hyperbolae-bounded embedding lattice region with no gaps. The corresponding sample joint distribution of the embedding window  $(m - 1)LT$  and the sample correlation dimension  $\hat{v}$ , as shown in Fig. 6(b), highlights, as in the Lorenz case, a uniformity region for embedding windows ranging from 0.245 to 0.455. It is worth noting that the resulting value of  $\hat{v}$  obtained by averaging the  $\hat{v}$  values within the uniformity region is equal to  $\hat{v}_2 = 2.30 \pm 0.02$ . This last value is

compatible with experimental and numerical assessments regarding Chua's circuit<sup>47</sup> that report—for different parameter settings, and without providing experimental errors—values between 2.13 and 2.42. A Kaplan–Yorke dimension of 2.13 was theoretically estimated for Chua's circuit;<sup>48</sup> the overestimation provided by the present approach might be due to the unavoidable presence of noise, which increases dimension estimates.

The optimal embedding criterion relying on mutual information and false nearest neighbors was also applied to the recorded potentials  $V_1$  and  $V_2$ . While a minimum of mutual information was identified at  $L = 7$  and  $L = 22$  for  $V_1$  and  $V_2$ , respectively, the fraction of false nearest neighbors did not reach zero within the analyzed range  $m = 2, \dots, 25$ . The identification of optimal dimensions  $m$  would thus require setting an arbitrary—and thus arguable—threshold, below which the fraction of false neighbors is deemed to be negligible.<sup>26</sup> The approach discussed in the present work, on the contrary, yields a set of suitable embedding points even when conventional methods fail to provide an unambiguous outcome.

## B. Resting state MEG recordings

The second case study concerns four MEG recordings of a human brain in the resting state. Data were downloaded from the public database of the Human Connectome Project (HCP).<sup>49,50</sup> The four recordings correspond to four sources of a single, multichannel MEG resting state acquisition carried out on a single subject. This subject was randomly chosen out of a set of 20 subjects analyzed in a former work by our group.<sup>51</sup> Details concerning the dataset and the related preprocessing steps can be found therein. Here, the four sequences corresponds to each one of the four human brain locations 10pp, V4, 5m, and STGa.<sup>51,52</sup> Current dipole amplitudes are reconstructed out of 300 s-long magnetic field recordings, yielding sequences comprising 75 000 elements each and sampled with  $T = 4$  ms.

Figure 7 shows the results of the analysis. The only appreciable difference between the four recordings concerns step 2: the regions that do not comply with the requirement  $v \leq m \leq \tau_1/(LT)$  are in all cases rectangular, though with different upper values of the embedding dimension  $m$ . This might have hinted at different chaotic behaviors in the four sources. However, the analysis of step 3 shows no region of uniform sample correlation dimension  $\hat{v}$  bounded by two hyperbolae. The absence of any uniformity region is also evident by the sample joint distributions of  $(m - 1)LT, \hat{v}$  for the correlation dimension maps shown in Fig. 8.

In summary, in the case of the four MEG recordings analyzed, there is no evidence of an underlying finite-dimensional, chaotic behavior. An alternative explanation is the inadequacy of the experimental recordings in terms of, for example, the bandwidth and signal-to-noise ratio. Moreover, it is known that detecting determinism in systems with high dimension ( $\gtrsim 5$ ) is hardly possible via time delay embedding because of the huge sample size required.<sup>53,54</sup> Systems of this kind are, for example, those relying on time-delayed feedback, whose fractal dimension can be arbitrarily large and for which alternative reconstruction approaches exist.<sup>55,56</sup>

## IV. CONCLUSIONS

In this paper, we described an approach that provides an additional tool<sup>34–36</sup> to tackle the longstanding issue of detecting chaos in time series analysis, especially whenever experimental series are concerned. The approach relies on an improved technique to identify optimal embedding pairs given an input scalar sequence and provide, if any, evidence of a finite-dimensional, chaotic behavior of the source generating the sequence.

## APPENDIX: DETAILS ON THE IMPLEMENTATION OF THE THREE EVALUATION STEPS

This appendix provides details on the implementation of the different steps outlined in Sec. II that make up the core of the approach discussed in this paper.

Given a standardized input sequence  $\{y_n\}$ , and given an embedding pair  $m, L$ , an embedding vector  $\mathbf{Y}_n$  is built as  $\mathbf{Y}_n = (y_n, y_{n+L}, \dots, y_{n+(m-1)L})$ . Given two embedding vectors  $\mathbf{Y}_i, \mathbf{Y}_j$ , their distance  $\delta_{ij}$  is evaluated according to a gauge-transformed metric based on the analytic expression of correlation integrals for GWN sequences

$$\delta_{ij} = \frac{1}{\Gamma(\frac{m}{2})} \gamma \left( \frac{m}{2}, \frac{1}{4} \|\mathbf{Y}_i - \mathbf{Y}_j\|^2 \right), \quad (\text{A1})$$

where  $\|\cdot\|$  is the Euclidean norm and  $\gamma(s, x)$  is the lower incomplete Gamma function. By virtue of the properties of this function,  $\delta_{ij}$  belongs to the interval  $[0, 1]$ .

A correlation integral  $\widehat{C}_{m,L}(\delta)$  is then computed as the sample cumulative distribution of the distance  $\delta$  in the set  $\{\mathbf{Y}_n\}$  of vectors that make up the embedded sequence

$$\widehat{C}_{m,L}(\delta) = \frac{1}{N} \sum_{\{i,j\}} \theta(\delta - \delta_{ij}),$$

where  $\theta(x)$  is the Heaviside theta function and the sum runs on a set  $\{i, j\}$  of  $N$  pairs of vectors. Vector pairs  $\{i, j\}$  are randomly extracted without replacement out of the embedded sequence. In order to avoid temporally correlated vectors, the random extraction is constrained to<sup>29,57</sup>  $|i - j| \geq c_0$ , where  $c_0$  is the largest between the second zero of the autocorrelation function and the product  $2m(L + 1)$ . In principle, a larger  $N$  allows for a better sampling of correlation integrals. However, in order to provide a reliable sampling,  $N$  should be chosen at least 2–3 orders of magnitude smaller than the number of available pairs, which is of order  $\ell^2/2$  ( $\ell$  is the length of the input sequence).<sup>29</sup> Moreover, computational costs have to be taken into account. Because the shortest sequence considered in this work has length  $\ell \sim 3 \times 10^4$ , in the present implementation  $N$  is set to 4000. A correlation bridge is finally obtained as

$$\widehat{B}_{m,L}(\delta) = \widehat{C}_{m,L}(\delta) - \delta.$$

### Step 1: Compatibility of a sequence with a GWN source

The assessment of the compatibility of an input sequence with a GWN source consists of testing whether a correlation

bridge is Brownian, i.e., whether  $\widehat{B}_{m,L}(\delta)$  is statistically compatible with the identically zero function. To this purpose, the Kolmogorov–Smirnov statistic  $\widehat{K}_{m,L;N}$  is first evaluated as

$$\widehat{K}_{m,L;N} = \sup_{\delta \in [0,1]} |\widehat{B}_{m,L}(\delta)|,$$

where  $N$  is the number of points making up the sample correlation bridge. In principle, compatibility can be assessed out of a single value of  $\widehat{K}_{m,L;N}$  by relying on the corresponding null hypothesis distribution<sup>58</sup>

$$F(K) = 1 - 2 \sum_{k=1}^{\infty} (-1)^{k-1} \exp(-2k^2 N' K^2),$$

where  $N' = (\sqrt{N} + 0.12 + 0.11/\sqrt{N})^2$ . However, to improve the assessment robustness as well as to avoid the evaluation of the infinite sum in the last expression, the computation of  $\widehat{K}_{m,L;N}$  is repeated  $M$  times. Each time, a correlation bridge is built by means of the random extraction procedure described above:  $M$  independent values of  $\widehat{K}_{m,L;N}$  are thus obtained. Thereupon, the sample mean  $\langle \widehat{K}_{m,L;N} \rangle$  is calculated. By virtue of the central limit theorem, if  $M \gg 1$  and under the null hypothesis that the input sequence is generated by a GWN source, the average is approximately distributed according to a normal distribution  $\mathcal{N}\left(\mu_K, \frac{\sigma_K^2}{M}\right)$ , where<sup>29</sup>

$$\mu_K = \sqrt{\frac{\pi}{2N'}} \ln 2,$$

$$\sigma_K = \sqrt{\frac{\pi}{2N'} \sqrt{\frac{\pi}{6} - \ln^2 2}}.$$

Given an average  $\langle \widehat{K}_{m,L;N} \rangle$ , the null hypothesis of a GWN source is then straightforwardly tested by computing the  $p$  value as

$$p = 1 - \Phi\left(\frac{\langle \widehat{K}_{m,L;N} \rangle - \mu_K}{\sigma_K/\sqrt{M}}\right),$$

where  $\Phi(z)$  is the standard normal cumulative distribution. In order to satisfy the requirements set by central limit theorem, in the present work  $M = 100$ .

## Step 2: Compatibility of the sequence with a finite-dimensional source

The assessment of the compatibility of an input sequence with a finite-dimensional source relies on the properties of correlation bridges at small distances, i.e., when the Grassberger–Procaccia scaling  $C_{m,L} = \beta_{m,L} r^v$  holds, where  $r$  is the Euclidean distance and  $\beta_{m,L}$  is an embedding-dependent constant. In this distance regime, it can be shown that the derivative of a correlation bridge  $B_{m,L}(\delta)$  turns out to be given by<sup>29</sup>

$$\frac{dB_{m,L}(\delta)}{d\delta} = \frac{v\beta_{m,L}}{2} \Gamma\left(\frac{m}{2}\right) \left(\frac{m}{4}\right)^{-m/2} \exp\left(\frac{mr^2}{4}\right) r^{v-m} - 1.$$

Consequently, if  $v < m$ , the derivative  $\frac{dB_{m,L}(\delta)}{d\delta}$  has to diverge to  $+\infty$  if  $r \rightarrow 0$ , i.e., if  $\delta \rightarrow 0$ . This property can be seen as a gauge-transformed, equivalent formulation of the Grassberger–Procaccia scaling, which also holds if  $v < m$ . In addition, as stated in Sec. II,

$m$  should not overcome an irrelevance-related limit, namely,  $m < \tau_l/(LT)$ .

The small-scale divergence is ascertained by means of a statistical approach, as follows.<sup>29</sup> As a result of the random extraction procedure described at the beginning of the present Appendix, a sample correlation bridge  $\widehat{B}_{m,L}(\delta)$  is made of  $N$  points, corresponding to  $N$  sampled values of distances  $\delta$ . The smallest one among these distances, which is referred to as  $\delta_1$ , corresponds to a “height” of the sample correlation bridge given by  $b_1 = 1/N - \delta_1$ . A number  $M$  of correlation bridges are built out of an input sequence, in analogy with step 1 and following the random extraction procedure described at the beginning of the present Appendix. For each one of these  $M$  correlation bridges, a value of  $b_1$  is evaluated. If any of the  $b_1$  values is vanishing or negative, a divergent behavior is deemed to be disproved. Otherwise, the probability of having a divergent behavior is determined via the Chebyshev inequality. First, the sample mean  $\bar{b}_1$  and sample standard deviation  $s_{b_1}$  of the  $M$  values of  $b_1$  are computed; thereupon, an upper bound to the probability  $P(b_1 \leq 0)$  of observing a negative  $b_1$  is estimated as<sup>29</sup>

$$P(b_1 \leq 0) \leq \left(\frac{s_{b_1}}{\bar{b}_1}\right)^2.$$

A small-scale divergent behavior of a sample correlation bridge is deemed to be disproved whenever  $(s_{b_1}/\bar{b}_1)^2$  overcomes a significance threshold set to 0.01.

Step 2 relies on the assessment of the sample mean  $\bar{b}_1$  and the sample standard deviation  $s_{b_1}$ . Reliable values of sample standard deviation, i.e., whose relative uncertainty is less than 0.1, require sample sets having a size of about 50. This size, on its turn, is sufficient to provide reliable values of sample means. As mentioned above, in this work the size  $M$  is set equal to 100.

## Step 3: Estimation of the sample correlation dimension

The third evaluation step relies on the estimation of the sample correlation dimension  $\widehat{\nu}$  out of the analysis of the asymptotic behavior of the time-dependent divergence exponent.<sup>30</sup> The sample time-dependent divergence exponent  $\Lambda(k)$  is defined as<sup>30,59</sup>

$$\widehat{\Lambda}(k) = \left\langle \log\left(\frac{\|\mathbf{Y}_{i+k} - \mathbf{Y}_{j+k}\|}{\|\mathbf{Y}_i - \mathbf{Y}_j\|}\right) \right\rangle,$$

where  $\|\cdot\|$  represents Euclidean distance and the pairs  $\mathbf{Y}_i, \mathbf{Y}_j$  of vectors are randomly selected so that their gauge-transformed distances  $\delta_{ij}$  satisfy  $\widehat{C}_{m,L}(\delta_{ij}) < p$ , i.e., belong to the  $p$ -th percentile of the distribution of distances.<sup>30,59</sup> It is worth reminding that percentiles are invariant under gauge transformations like that of Eq. (A1), regardless of the  $m$  value.

For sufficiently large values of  $k$ , the divergence exponent  $\widehat{\Lambda}(k)$  reaches a saturation value  $\Lambda_{pl}$ , referred to as a “plateau.”<sup>30</sup> In the case of a chaotic source of finite correlation dimension  $\nu$ , the plateau  $\Lambda_{pl}$  turns out to linearly depend on the logarithm of the percentile  $p$ ,

$$\Lambda_{pl} = \Lambda' - \frac{1}{\nu} \log(p), \quad (A2)$$

where  $\Lambda'$  is an embedding-dependent constant. The dependence expressed by Eq. (A2) can thus be exploited to estimate, if any, the sample correlation dimension  $\hat{\nu}$  out of an input scalar sequence by carrying out a linear fit on a set of  $(\log(p), \hat{\Lambda}_{pl})$  data points.

Concerning a single data point, given a percentile  $p$ , the assessment of the related  $\hat{\Lambda}_{pl}$  requires three steps. First, the evaluation of  $\hat{\Lambda}(k)$  for a set of sufficiently large  $k$  values so that they lay within the plateau. Second, the fit of a constant to this set of  $\hat{\Lambda}(k)$ 's. The related  $\chi^2$  test allows to check the goodness of the selection of the set of  $k$  values.<sup>30</sup> Third, the repetition of the first two steps a number  $M$  of times. The final values of  $\hat{\Lambda}_{pl}$  corresponds to the average of the  $M$  results of the fit with a constant value. In this work,  $M = 10$ .

Once a set of  $(\log(p), \hat{\Lambda}_{pl})$  data points is at hand, a linear fit is carried out on the set. As a rule of thumb, at least four data points are required with the percentile  $p$  spanning at least two decades in order to get relative uncertainties on the  $\hat{\nu}$  assessment below 0.1. In this work, in the case of the Lorenz sequence, eight data points were considered with  $p$  ranging from  $10^{-4}$  to 0.3. With regard to Chua's circuit, five points were considered, with  $p$  ranging from  $3 \times 10^{-3}$  to 0.3. Finally, in the case of MEG recordings, six points were considered, with  $p$  ranging from  $10^{-3}$  to 0.3.

## Computational costs

The computations presented in this work were carried out by using a 20-core cluster node hosting two Intel® Xeon® E5-2650V3 CPUs with 256 GB RAM, running Linux CentOS 7 64-bit. Codes are written in C++ and compiled via the GNU Compiler Collection<sup>60</sup> version 4.8.5 by setting the optimization flag to **-O3**. The complete evaluation of an embedding point takes a time that is approximately proportional to the product  $mL$ , i.e., to the embedding window. As a reference, the computation of the lattice of Fig. 1 concerning a Lorenz sequence made of  $10^5$  points required 9 min for the embedding point  $m, L = 2, 1$ . The time increased to 25 min for the embedding point  $10, 10$ , and reached 257 min for the embedding point  $20, 10$ .

## DATA AVAILABILITY

Data used in the first example concerning Chua's circuit are available from the corresponding author upon reasonable request. Data used in the second example concerning MEG recordings in the resting state are openly available in Human Connectome Project (HPC) at <https://db.humanconnectome.org/>, Ref. 20.

## REFERENCES

- <sup>1</sup>A. A. Tsonis and J. B. Elsner, "Chaos, strange attractors, and weather," *Bull. Am. Meteorol. Soc.* **70**, 14–23 (1989).
- <sup>2</sup>C. L. Keppenne and C. Nicolis, "Global properties and local structure of the weather attractor over Western Europe," *J. Atmos. Sci.* **46**, 2356–2370 (1989).
- <sup>3</sup>J. Slingo and T. Palmer, "Uncertainty in weather and climate prediction," *Phil. Trans. R. Soc.* **369**, 4751–4767 (2011).
- <sup>4</sup>W. A. Barnett and A. Serletis, "Martingales, nonlinearity, and chaos," *J. Econ. Dyn. Control* **24**, 703–724 (2000).
- <sup>5</sup>W. A. Barnett, A. Serletis, and D. Serletis, "Nonlinear and complex dynamics in economics," *Macroecon. Dyn.* **19**, 1749–1779 (2015).
- <sup>6</sup>H. Hayashi, M. Nakao, and K. Hirakawa, "Chaos in the self-sustained oscillation of an excitable biological membrane under sinusoidal stimulation," *Phys. Lett. A* **88**, 265–266 (1982).
- <sup>7</sup>H. Hayashi and S. Ishizuka, "Chaotic nature of bursting discharges in the Onchidium pacemaker neuron," *J. Theor. Biol.* **156**, 269–291 (1992).
- <sup>8</sup>L. Glass, M. R. Guevara, A. Shrier, and R. Perez, "Bifurcation and chaos in a periodically stimulated cardiac oscillator," *Physica D* **7**, 89–101 (1983).
- <sup>9</sup>R. B. Govindan, K. Narayanan, and M. S. Gopinathan, "On the evidence of deterministic chaos in ECG: Surrogate and predictability analysis," *Chaos* **8**, 495–502 (1998).
- <sup>10</sup>T. Henriques, M. Ribeiro, A. Teixeira, L. Castro, L. Antunes, and C. Costa-Santos, "Nonlinear methods most applied to heart-rate time series: A review," *Entropy* **22**, 309 (2020).
- <sup>11</sup>A. Babloyantz, J. M. Salazar, and C. Nicolis, "Evidence of chaotic dynamics of brain activity during the sleep cycle," *Phys. Lett. A* **111**, 152–156 (1985).
- <sup>12</sup>J. Fell, J. Röschke, and P. Beckmann, "Deterministic chaos and the first positive Lyapunov exponent: A nonlinear analysis of the human electroencephalogram during sleep," *Biol. Cybern.* **69**, 139–146 (1993).
- <sup>13</sup>K. Lehnertz and C. E. Elger, "Spatio-temporal dynamics of the primary epileptogenic area in temporal lobe epilepsy characterized by neuronal complexity loss," *Electroen. Clin. Neuro.* **95**, 108–117 (1995).
- <sup>14</sup>H. D. I. Abarbanel, R. Brown, J. J. Sidorowich, and L. S. Tsimring, "The analysis of observed chaotic data in physical systems," *Rev. Mod. Phys.* **65**, 1331–1392 (1993).
- <sup>15</sup>J. Theiler, "Estimating fractal dimension," *J. Opt. Soc. Am. A* **7**, 1055–1073 (1990).
- <sup>16</sup>J. Gao and Z. Zheng, "Local exponential divergence plot and optimal embedding of a chaotic time series," *Phys. Lett. A* **181**, 153–158 (1993).
- <sup>17</sup>M. T. Rosenstein, J. J. Collins, and C. J. De Luca, "A practical method for calculating largest Lyapunov exponents from small data sets," *Physica D* **65**, 117–134 (1993).
- <sup>18</sup>H. Kantz, "A robust method to estimate the maximal Lyapunov exponent of a time series," *Phys. Lett. A* **185**, 77–87 (1994).
- <sup>19</sup>P. Grassberger and I. Procaccia, "Characterization of strange attractors," *Phys. Rev. Lett.* **50**, 346–349 (1983).
- <sup>20</sup>P. Grassberger and I. Procaccia, "Measuring the strangeness of strange attractors," *Physica D* **9**, 189–208 (1983).
- <sup>21</sup>J. L. Kaplan and J. A. Yorke, "Chaotic behavior of multidimensional difference equations," in *Functional Differential Equations and Approximations of Fixed Points*, Lecture Notes in Mathematics Vol. 730, edited by H. O. Peitgen and H. O. Walther (Springer, Berlin, 1979), pp. 204–227.
- <sup>22</sup>P. Frederickson, J. L. Kaplan, E. D. Yorke, and J. A. Yorke, "The Liapunov dimension of strange attractors," *J. Differ. Equ.* **49**, 185–207 (1983).
- <sup>23</sup>F. Takens, "Detecting strange attractors in turbulence," in *Dynamical Systems and Turbulence, Warwick 1980*, Lecture Notes in Mathematics Vol. 898, edited by D. Rand and L. S. Young (Springer, Berlin, 1981), pp. 366–381.
- <sup>24</sup>T. Sauer, J. A. Yorke, and M. Casdagli, "Embedology," *J. Stat. Phys.* **65**, 579–616 (1991).
- <sup>25</sup>N. H. Packard, J. P. Crutchfield, J. D. Farmer, and R. S. Shaw, "Geometry from a time series," *Phys. Rev. Lett.* **45**, 712–716 (1980).
- <sup>26</sup>C. J. Cellucci, A. M. Albano, and P. E. Rapp, "Comparative study of embedding methods," *Phys. Rev. E* **67**, 066210 (2003).
- <sup>27</sup>L. M. Pecora, L. Moniz, J. Nichols, and T. L. Carroll, "A unified approach to attractor reconstruction," *Chaos* **17**, 013110 (2007).
- <sup>28</sup>D. Kugiumtzis, "State space reconstruction parameters in the analysis of chaotic time series—The role of the time window length," *Physica D* **95**, 13–28 (1996).
- <sup>29</sup>A. Perinelli and L. Ricci, "Identification of suitable embedding dimensions and lags for time series generated by chaotic, finite-dimensional systems," *Phys. Rev. E* **98**, 052226 (2018).
- <sup>30</sup>L. Ricci, A. Perinelli, and M. Franchi, "Asymptotic behavior of the time-dependent divergence exponent," *Phys. Rev. E* **101**, 042211 (2020).
- <sup>31</sup>M. Casdagli, S. Eubank, J. D. Farmer, and J. Gibson, "State space reconstruction in the presence of noise," *Physica D* **51**, 52–98 (1991).
- <sup>32</sup>E. N. Lorenz, "Deterministic nonperiodic flow," *J. Atmos. Sci.* **20**, 130–141 (1963).
- <sup>33</sup>E. Bradley and H. Kantz, "Nonlinear time-series analysis revisited," *Chaos* **25**, 097610 (2015).
- <sup>34</sup>H. Kantz and T. Schreiber, *Nonlinear Time Series Analysis*, 2nd ed. (Cambridge University Press, Cambridge, UK, 2003).

- <sup>35</sup>R. Hegger, H. Kantz, and T. Schreiber, "Practical implementation of nonlinear time series methods: The TISEAN package," *Chaos* **9**, 413–435 (1999).
- <sup>36</sup>See [https://www.pks.mpg.de/tisean/Tisean\\_3.0.1/](https://www.pks.mpg.de/tisean/Tisean_3.0.1/) for "TISEAN" (last accessed September 2020).
- <sup>37</sup>J. C. Sprott and G. Rowlands, "Improved correlation dimension calculation," *Int. J. Bifurcat. Chaos* **11**, 1865–1880 (2001).
- <sup>38</sup>A. Namajūnas, K. Pyragas, and A. Tamasevičius, An electronic analog of the Mackey-Glass system," *Phys. Lett. A* **201**, 42–46 (1995).
- <sup>39</sup>B. Muthuswamy, "Implementing memristor based chaotic circuits," *Int. J. Bifurcat. Chaos* **20**, 1335–1350 (2010).
- <sup>40</sup>L. Minati, M. Frasca, P. Oświęcimka, L. Faes, and S. Drożdż, "Atypical transistor-based chaotic oscillators: Design, realization, and diversity," *Chaos* **27**, 073113 (2017).
- <sup>41</sup>L. Minati, M. Frasca, G. Giustolisi, P. Oświęcimka, S. Drożdż, and L. Ricci, "High-dimensional dynamics in a single-transistor oscillator containing Feynman-Sierpiński resonators: Effect of fractal depth and irregularity," *Chaos* **28**, 093112 (2018).
- <sup>42</sup>L. Minati, M. Frasca, N. Yoshimura, L. Ricci, P. Oświęcimka, Y. Koike, K. Masu, and H. Ito, "Current-starved cross-coupled CMOS inverter rings as versatile generators of chaotic and neural-like dynamics over multiple frequency decades," *IEEE Access* **7**, 54638–54657 (2019).
- <sup>43</sup>L. Minati, L. V. Gambuzza, W. J. Thio, J. C. Sprott, and M. Frasca, "A chaotic circuit based on a physical memristor," *Chaos Soliton. Fract.* **138**, 109990 (2020).
- <sup>44</sup>R. N. Madan, *Chua's Circuit: A Paradigm for Chaos* (World Scientific, 1993).
- <sup>45</sup>T. Matsumoto, "A chaotic attractor from Chua's circuit," *IEEE T. Circuits Syst.* **31**, 1055–1058 (1984).
- <sup>46</sup>See [www.analog.com/media/en/technical-documentation/data-sheets/OP07.pdf](http://www.analog.com/media/en/technical-documentation/data-sheets/OP07.pdf) for "The OP-07 Datasheet" (last accessed September 2020).
- <sup>47</sup>H. A. Albuquerque, R. M. Rubinger, and P. C. Rech, "Theoretical and experimental time series analysis of an inductorless Chua's circuit," *Physica D* **233**, 66–72 (2007).
- <sup>48</sup>T. Matsumoto, L. O. Chua, and M. Komuro, "The double scroll," *IEEE T. Circuits Syst.* **32**, 797–818 (1985).
- <sup>49</sup>D. C. Van Essen, S. M. Smith, D. M. Barch, T. E. J. Behrens, E. Yacoub, and K. Ugurbil, "The WU-Minn human connectome project: An overview," *Neuroimage* **80**, 62–79 (2013).
- <sup>50</sup>See <https://db.humanconnectome.org/> for Dataset reference: WU-Minn HCP Data – 1200 Subjects.
- <sup>51</sup>A. Perinelli, D. Tabarelli, C. Miniussi, and L. Ricci, "Dependence of connectivity on geometric distance in brain networks," *Sci. Rep.* **9**, 13412 (2019).
- <sup>52</sup>M. F. Glasser, T. S. Coalson, E. C. Robinson, C. D. Hacker, J. Harwell, E. Yacoub, K. Ugurbil, J. Andersson, C. F. Beckmann, M. Jenkinson, S. M. Smith, and D. C. Van Essen, "A multi-modal parcellation of human cerebral cortex," *Nature* **536**, 171–178 (2016).
- <sup>53</sup>E. Olbrich and H. Kantz, "Inferring chaotic dynamics from time-series: On which length scale determinism becomes visible," *Phys. Lett. A* **232**, 63–69 (1997).
- <sup>54</sup>H. Kantz and E. Olbrich, "Scalar observations from a class of high-dimensional chaotic systems: Limitations of the time delay embedding," *Chaos* **7**, 423–429 (1997).
- <sup>55</sup>M. J. Bünnér, M. Ciofini, A. Giaquinta, R. Hegger, H. Kantz, R. Meucci, and A. Politi, "Reconstruction of systems with delayed feedback: I. Theory," *Eur. Phys. J. D* **10**, 165–176 (2000).
- <sup>56</sup>M. J. Bünnér, M. Ciofini, A. Giaquinta, R. Hegger, H. Kantz, R. Meucci, and A. Politi, "Reconstruction of systems with delayed feedback: II. Application," *Eur. Phys. J. D* **10**, 177–187 (2000).
- <sup>57</sup>J. Theiler, "Spurious dimension from correlation algorithms applied to limited time-series data," *Phys. Rev. A* **34**, 2427–2432 (1986).
- <sup>58</sup>W. H. Press, S. A. Teukolsky, W. T. Vetterling, and B. P. Flannery, *Numerical Recipes. The Art of Scientific Computing*, 3rd ed. (Cambridge University Press, 2007).
- <sup>59</sup>M. Franchi and L. Ricci, "Statistical properties of the maximum Lyapunov exponent calculated via the divergence rate method," *Phys. Rev. E* **90**, 062920 (2014).
- <sup>60</sup>See <https://gcc.gnu.org/> for "GCC" (last accessed September 2020).